CONVOLUTION BACK-PROJECTION IMAGING ALGORITHM FOR DOWNWARD-LOOKING SPARSE LINEAR ARRAY THREE DIMENSIONAL SYNTHETIC APERTURE RADAR

X. M. Peng[*], W. X. Tan, Y. P. Wang, W. Hong, and Y. R. Wu

Science and Technology on Microwave Imaging Laboratory, Institute of Electronics, Chinese Academy of Sciences, Beijing 100190, China

Abstract—General side-looking synthetic aperture radar (SAR) cannot obtain scattering information about the observed scenes which are constrained by lay over and shading effects. Downward-looking sparse linear array three-dimensional SAR (DLSLA 3D SAR) can be placed on small and mobile platform, allows for the acquisition of full 3D microwave images and overcomes the restrictions of shading and lay over effects in side-looking SAR. DLSLA 3D SAR can be developed for various applications, such as city planning, environmental monitoring, Digital Elevation Model (DEM) generation, disaster relief, surveillance and reconnaissance, etc. In this paper, we give the imaging geometry and dechirp echo signal model of DLSLA 3D SAR. The sparse linear array is composed of multiple transmitting and receiving array elements placed sparsely along cross-track dimension. The radar works on time-divided transmitting-receiving mode. Particularly, the platform motion impact on the echo signal during the time-divided transmitting-receiving procedure is considered. Then we analyse the wave propagation, along-track and cross-track dimensional echo signal bandwidth before and after dechrip processing. In the following we extend the projection-slice theorem which is widely used in computerized axial tomography (CAT) to DLSLA 3D SAR imaging. In consideration of the flying platform motion compensation during time-divided transmitting-receiving procedure and parallel implementation on multi-core CPU or Graphics processing units (GPU) processor, the convolution back-projection (CBP) imaging algorithm is proposed for DLSLA 3D SAR image reconstruction. At last, the focusing capabilities

of our proposed imaging algorithm are investigated and verified by numerical simulations and theoretical analysis.

1. INTRODUCTION

Owing to side-looking geometry in general SAR systems, shading and lay over effects by trees, buildings, special terrain shapes will hide essential information of the observed areas, particularly in urban areas and deep valleys in mountain areas [1–3]. DLSLA 3D SAR acquires full 3D microwave images by wave propagation dimensional pulse compression, along-track dimensional aperture synthesis with flying platform movement and cross-track dimensional aperture synthesis with a sparse linear array [4]. And DLSLA 3D SAR observes nadir areas which means it overcomes restrictions of shading and lay over effects in side-looking SAR.

Downward-Looking Imaging Radar (DLIR) [5] was first introduced by Gierull in 1999. He took advantage of aperture synthesis by platform movement along along-track dimension and linear array aperture synthesis along cross-track dimension to form a two dimensional aperture and transmitted a single frequency signal to obtain the two dimensional image. Nouvel et al. in ONERA [6–8] made use of chirp signal instead of single frequency signal and developed the concept of downward-looking 3D-SAR and developed a Ka band linear array 3D-SAR system. Researchers in FGAN-FHR designed an Airborne Radar for Three-dimensional Imaging and Nadir Observation (ARTINO) [4, 9]. The system places a thinned linear array along cross-track dimension, it obtains three dimensional resolution by wave propagation pulse compression, aperture synthesis along the fly dimension and beam-forming along cross-track dimension. The imaging algorithms of the two systems are not illustrated in detail and the 3D imaging results of the two systems have not been publicly reported yet [10].

DLSLA 3D SAR requires pretty fast A/D sampling devices and pretty high capacity data collection devices for echo data recording as there are more transmitting-receiving channels in DLSLA 3D SAR than in side-looking SAR. Sparse linear array with the time-divided transmitting-receiving is often applied to the 3D SAR which helps to reduce the complexity of the system. The motion of the platform during the time-divided transmitting-receiving procedure degrades the reconstructed image and the motion effect should be compensated in the imaging algorithm. Most of the published imaging algorithms suppose the echo signal without carrier frequency and be digitized directly, and take no consideration of A/D sampling

rate limitation, echo data voxel volume and flying platform motion effect during the time-divided transmitting-receiving procedure. These algorithms mainly get the wave propagation and along-track dimension compression first with Range Doppler algorithm, Chirp Scaling algorithm and Range Migration algorithm like general two dimensional SAR image reconstruction, then obtain the cross-track dimension compression via SPECAN, beam-forming, CS (Compressed Sensing), etc. [11–16]. These algorithms may be suited for multi-baseline 3D SAR whose echo signal is composed of two dimensional general SAR echo signal along multi-baseline. Multi-baseline 3D SAR systems put less burden on A/D sampling devices and data collection devices while require quite a long time to obtain the 3D echo signal, and the sampling interval between the multi-baseline is not uniform [13, 15, 16], which restricts the imaging algorithms on the basis of uniform Nyquist sampling theorem. What's more, any change of the imaging scene destroys the coherence of the imaging scene, while the coherence of the imaging scene is very important for microwave imaging [2].

The dechirp signal processing technique is mainly used in spotlight mode SAR systems which helps to reduce the echo signal bandwidth. Dechirp signal processing technique mixes the echo signal with a reference function which is the echo signal from APC (Antenna Phase Center) to SC (Scene Center) [2]. The reduced bandwidth is only related to the range extension of the imaging scene. DLSLA 3D SAR operates in nadir observation. And in wave propagation dimension, the range gate is the undulation range of the imaging scene. This range gate is several hundred meters in urban areas or plane areas, and the corresponding range gate time delay is very small. While, the pulse of the transmitting signal is often larger than the range gate time delay in order to obtain enough echo power and echo SNR. So the dechirp signal processing technique is very suitable for DLSLA 3D SAR for which helps to reduce the A/D sampling bandwidth and echo data volume. Our work below is based on dechirp processing technique. Projection-slice theorem was introduced and used in CAT first [17]. Later, some researchers extended projection-slice theorem to spotlight mode SAR image reconstruction [18, 19]. Knaell and Cardillo [20] discussed the radar tomography for the generation of three-dimensional images, but they neglected the center frequency shift of the convolution kernel, and they did not give the cross-track dimensional imaging geometry and the three dimensional point spread function. What's more, the algorithm they introduced takes no consideration of the platform motion effect during the time-divided transmitting-receiving procedure which means it cannot be used for DLSLA 3D SAR imaging. In this paper, we offer a new point of view to DLSLA 3D SAR echo signal acquisition on the

basis of projection-slice theorem. And, the CBP imaging algorithm which compensates the flying platform motion effect during the time-divided transmitting-receiving procedure and contains the advantage of parallel implementation [21, 22], is introduced for DLSLA 3D SAR.

The structure of this paper is organized as follows. Downward-looking sparse linear array 3D SAR imaging geometry, echo signal model, platform motion effect during time-divided transmitting-receiving procedure and echo signal bandwidth before and after dechirp are established in Section 2; then, in Section 3, projection-slice theorem and its application in DLSLA 3D SAR are described in detail; CBP imaging algorithm with platform motion compensation during time-divided transmitting-receiving procedure and the parallel implementation of the algorithm is discussed in Section 4; Section 5 gives some computer simulations and result analysis. Finally, conclusion is provided in Section 6.

2. DOWNWARD-LOOKING SPARSE LINEAR ARRAY THREE DIMENSIONAL SAR IMAGING GEOMETRY AND ECHO MODEL

This section is splitted into four subsections. First, we give the DLSLA 3D SAR imaging geometry and illustrate why DLSLA 3D SAR can gather three dimensional scatter information that avoided shading and lay over effects. Then the echo signal model with dechirp signal processing technique is introduced. Next the platform motion effect during the time-divided transmitting-receiving procedure is analyzed. At last, the echo signal bandwidth in every dimension before and after dechirp processing is analysed.

2.1. Downward-looking Sparse Linear Array Three Dimensional SAR Imaging Geometry

As is shown in Fig. 1. X-axis is parallel to the flight path of the platform, Y-axis is parallel to the cross-track dimensional sparse linear array, Z-axis is perpendicular to the XY plane, the origin of the coordinate O is the center of the three dimensional imaging scene (O is also used as the reference point for dechirp signal processing). Q is the Antenna Phase Center (APC), Q' is the projection point of Q on XY plane, P is the target in the imaging scene. APC flight path $\overrightarrow{QX'}$ is parallel to X-axis. $\overrightarrow{QO}$ is the instantaneous reference range from APC to SC with the distance of R_0, $\overrightarrow{OP}$ is the instantaneous range from SC to target with the distance of R, $\overrightarrow{QP}$ is the instantaneous slant
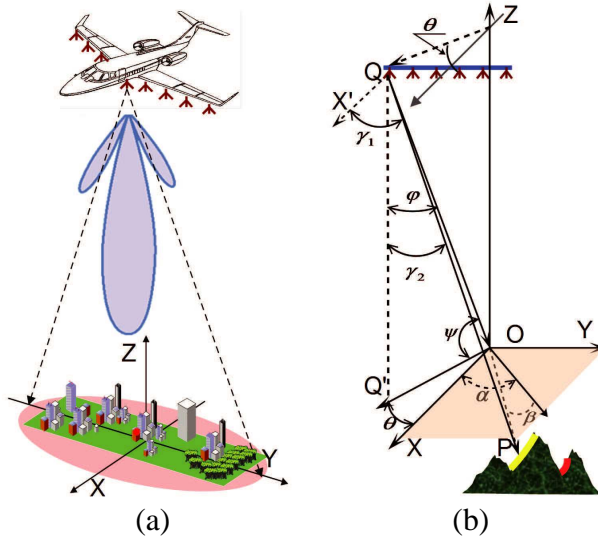
Figure 1. DLSLA 3D SAR imaging mode and imaging geometry. (a) DLSLA 3D SAR imaging mode. (b) DLSLA 3D SAR imaging geometry.

range from APC to target with the distance of R_t. $\overrightarrow{QP} = \overrightarrow{QO} + \overrightarrow{OP}$ ($R_t = R_0 + R$) on the hypothesis of planar wave front. ψ is the angle between $\overrightarrow{OQ}$ and XY plane, called as *grazing angle*. φ is the angle between $\overrightarrow{OQ}$ and Z-axis, called as *incident angle*. θ is the angle between $\overrightarrow{OQ'}$ and X-axis, called as *slant angle*. γ_1 is the angle between $\overrightarrow{QX'}$ and $\overrightarrow{QP}$, called as *along-track dimension Doppler cone angle*. γ_2 is the angle between $\overrightarrow{QQ'}$ and $\overrightarrow{QP}$, called as *cross-track dimension Doppler cone angle*.

The SAR processor needs three kinds of information to reconstruct an image from sensor signals. First, it needs positioning information to locate the source of the return echoes in the imaging scene. Second, it needs spatial or angular resolution information to differentiate among return echoes from separate scatters or scene areas. Finally, it needs the intensity information of the signal associated with each other or scene areas in the target field. In the case of radar, the intensity is the radar cross section of individual scatter or the radar backscatter coefficient of distributed areas [2]. As shown in Fig. 1, general side-looking SAR measures range from APC to target and along-track Doppler cone angle γ_1. It can not distinguish targets on the yellow

region as they have the same range and the same along-track Doppler cone angle [3]. And grazing angle in side-looking SAR is small, especially in the far range gate unit, the red region is shaded by other targets, and SAR sensor can not obtain scattering information of this region [3]. DLSLA 3D SAR measures range from APC to target, along-track dimension Doppler cone angle γ_1, cross-track dimension Doppler cone angle γ_2 and the radar cross section of the imaging scene which means it acquires full 3D microwave image of the observed areas. And, DLSLA 3D SAR operates nadir observation, therefore, layover and shading effects can be overcome.

2.2. Downward-looking Sparse Linear Array Three Dimensional SAR Imaging Echo Model

The sparse linear array is composed of multiple transmitting array elements and multiple receiving array elements placed sparsely along the cross-track dimension and works on the time-divided transmitting-receiving mode. According to the equivalent phase center theorem, the sparse linear array with multiple transmitting array elements and multiple receiving array elements on the basis of time division can be equivalent to a uniform linear array that every equivalent array element transmits and receives signal by itself [12]. All the equations below are based on the equivalent phase center theorem as the range from APC to target is large enough that the phase error generated by equivalent phase center theorem can be ignored. The sparse linear array we design is based on ARTINO array distribution [3] as the length of equivalent array with this method is longer than other methods [23, 24]. What's more, ARTINO array distribution is quite easy for hardware implementation [25]. Suppose that there are L_1 transmitting array elements, L_2 receiving array elements. The equivalent phase center number is $L_1 L_2$ according to ARTINO array distribution [3]. A chirp signal with carrier frequency f_c, chirp rate K_r, pulse width T_p is transmitted and received. The transmitted signal can be written as

$$S(m, n, t) = \text{rect}\left(\frac{\hat{t}}{T_p}\right) \exp\left\{j\left[2\pi f_c t + \pi K_r \hat{t}^2\right]\right\}, \tag{1}$$

where m is the cross-track dimensional equivalent array element number, n is the along-track dimensional pulse number and $\hat{t}$ is fast time. Here we are going to develop an equation for the signal phase received by DLSLA 3D SAR system from a single scatter object P at scene coordinate (x, y, z). This development assumes an ideal point scatter object with radar cross section σ whose amplitude and phase characteristics do not vary with frequency and aspect angle. For simplicity, the receiving signal model ignores antenna gain, amplitude

effects of propagation on the signal and any additional time delays due to atmospheric effects. The signal received from target P at array element number m and pulse number n is

$$S_r(m, n, t) = a_t \text{rect} \left(\frac{\hat{t} - t_d}{T_p} \right) \exp \left\{ j \left[2\pi f_c(t - t_d) + \pi K_r \left(\hat{t} - t_d \right)^2 \right] \right\}, \quad (2)$$

where $a_t = \sqrt{\sigma}$, $t_d = \frac{2R_t}{c}$ is the dual time delay from APC to target P. It is appropriate to view the received signal as a three dimensional signal in the coordinates m, n and $\hat{t}$. The reference receiving signal from APC to reference point at SC, O, is

$$S_{\text{ref}}(m, n, t) = \exp \left\{ j \left[2\pi f_c(t - t_0) + \pi K_r \left(\hat{t} - t_0 \right)^2 \right] \right\}, \quad (3)$$

where $t_0 = \frac{2R_0}{c}$ is the dual time delay from APC to reference point at scene center O. The radar receiving signal is the video frequency signal generated by mixing the received signal from target P with reference received signal from reference point O. It is convenient to write the video frequency echo signal in the form

$$\begin{aligned} S_{\text{if}}(m, n, t) &= S_r(m, n, t) \times S_{\text{ref}}^*(m, n, t) \\ &= a_t \text{rect} \left(\frac{\hat{t} - t_d}{T_p} \right) \exp \left\{ j\Phi \left(m, n, \hat{t} \right) \right\}. \end{aligned} \quad (4)$$

The phase term $\Phi(m, n, \hat{t})$ in Eq. (4) can be written as,

$$\Phi \left(m, n, \hat{t} \right) = -KR + \frac{4\pi K_r}{c^2} R^2, \quad (5)$$

where

$$R = R_t - R_0.$$

In Eq. (5), $K = \frac{4\pi K_r}{c} \left(\frac{f_c}{K_r} + \hat{t} - \frac{2R_0}{c} \right)$ and $\exp \left\{ j \frac{4\pi K_r}{c^2} R^2 \right\}$ is the Residual Video Phase (RVP) term. The RVP term is the consequence of dechirp-on-receive approach. It can be completely removed from the radar echo signal by a preprocessing operation which is illustrated in Appendix A.

2.3. Platform Motion Effects During Time-divided Transmitting-receiving Procedure

Now, we run back over the echo data collection procedure. The sparse linear array maintains multiple transmitting array elements and multiple receiving array elements and the sparse array works in time-divided mode. As shown in Fig. 2, There are L_1 transmitting array elements and L_2 receiving array elements. The transmitting array elements work sequentially, array element T_1 transmits signal first,

all the receiving array elements receive echo signal simultaneously and L_2 equivalent array elements are obtained, the time interval of this transmitting and receiving procedure is ΔT. Then array element T_2 transmits signal, and the procedure loops until array element T_{L1} finishes transmitting signal. Finally the radar obtains $L_1 L_2$ equivalent array elements. The cross-track dimensional equivalent element number $m \in [1, L_1 L_2]$ in the video frequency echo signal $S_{\mathrm{if}}(m, n, t)$. The echo data collection procedure is shown in Fig. 2.

As the radar works in the time division mode, the whole transmitting and receiving procedure of the sparse linear array is not short enough to be treated under stop-and-go approximation. The platform motion during the time-divided transmitting-receiving procedure should be considered in the video frequency echo signal $S_{\mathrm{if}}(m, n, t)$. As shown in Fig. 3, O is the SC with coordinates $(0, 0, 0)$. The platform movement is $\Delta x = l \times V \times \Delta T$, where l means array element T_l transmits signal, V is flying platform velocity. The coordinates of APC is $(x_i + \Delta x, y_i, z_i)$. The coordinates of target P is (x, y, z). The range between scene center and APC is R_0, the range between target and APC is R_t, where

$$R_0 = \sqrt{(x_i + \Delta x)^2 + r_0^2}$$

$$R_t = \sqrt{[(x_i + \Delta x) - x]^2 + r_t^2}, \tag{6}$$

and where $r_0 = \sqrt{y_i^2 + z_i^2}$, $r_t = \sqrt{(y - y_i)^2 + (z - z_i)^2}$, then making the substitution (without considering RVP) and taking along-track
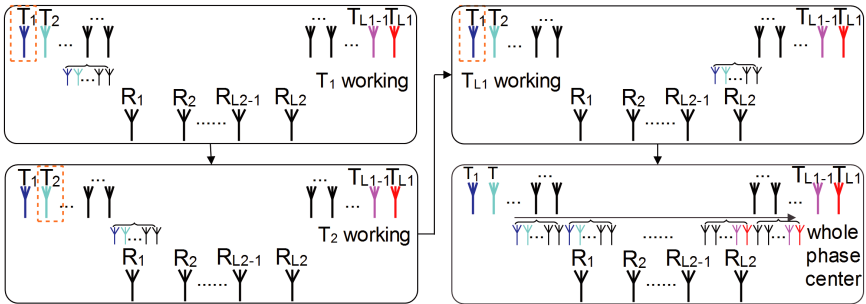

Figure 2. Time divided MIMO echo data collection.
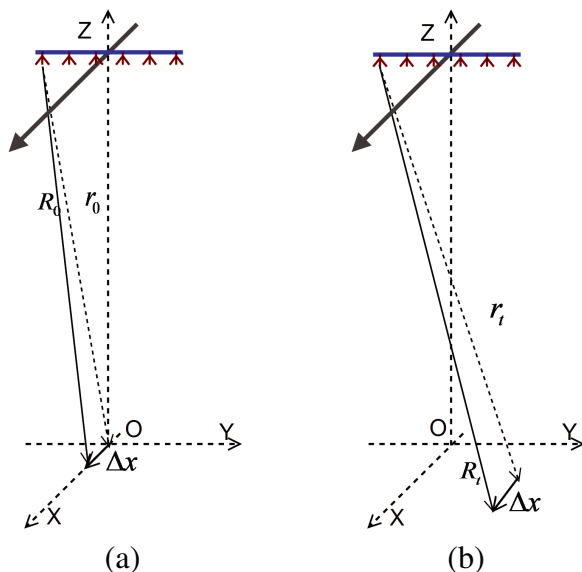
Figure 3. Reference and instantaneous range with platform motion. (a) Reference range. (b) Instantaneous range.

dimensional Fourier transform, we obtain

$$
\begin{aligned}
F_x \left\{ S_{\mathrm{if}}(m,n,t) \right\} &= \int_x S_{\mathrm{if}}(m,n,t) \exp\left\{ -jK_x x_i \right\} dx_i \\
&= A_0 \int_x \exp\left\{ -jKR \right\} \exp\left\{ -jK_x x_i \right\} dx_i \\
&= A_1 \exp\left\{ jK_x \Delta x \right\} \exp\left\{ j\sqrt{K^2 - K_x^2}(r_t - r_0) - jK_x x \right\}, \quad (7)
\end{aligned}
$$

where

$$
R = R_t - R_0 = \sqrt{r_t^2 + [(x_i + \Delta x) - x]^2} - \sqrt{r_0^2 + (x_i + \Delta x)}.
$$

and A_0 and A_1 are the corresponding amplitudes before and after Fourier transform.

Equation (7) describes the platform motion during the time-divided transmitting-receiving procedure causes an along-track dimensional phase term, this phase term should be compensated in image reconstruction procedure.

2.4. Echo Signal Bandwidth Before and after Dechirp Processing

As shown in Fig. 4, the AD sampling begins at the same time as the dechirp starts. The video signal is digitized by the AD converter. Corresponding to the return of the center of the pulse from the quantized reference range R_0, the AD trigger for the first sample steps back by $T_p/2$ to the start of the pulse and steps back $T_s/2$ to the start of the range window. The total sampling time is $T_p + T_s$.

The AD converter samples the video signal at fast time $\hat{t}_s(m, n, k)$:

$$\hat{t}_s(m, n, k) = \frac{k}{F_s} + \frac{2R_0}{c} - \frac{T_p}{2} - \frac{T_s}{2}. \tag{8}$$

Eq. (8) describes the value of a sample of the array element m, along-track pulse n and wave-propagation dimension sample k. F_s is the sampling frequency, $T_s = \frac{2R}{c} = \frac{4\Delta R}{c}$ is the time interval associated with the wave-propagation dimensional range gate $R(R \in [-\Delta R, \Delta R])$. The phase of the signal from APC sample cell (m, n, k) to target P is

$$\Phi(m, n, k) = -\frac{4\pi K_r}{c} \left(\frac{f_c}{K_r} + \frac{k}{F_s} - \frac{T_p}{2} - \frac{T_s}{2} \right) R + \frac{4\pi K_r}{c^2} R^2. \tag{9}$$
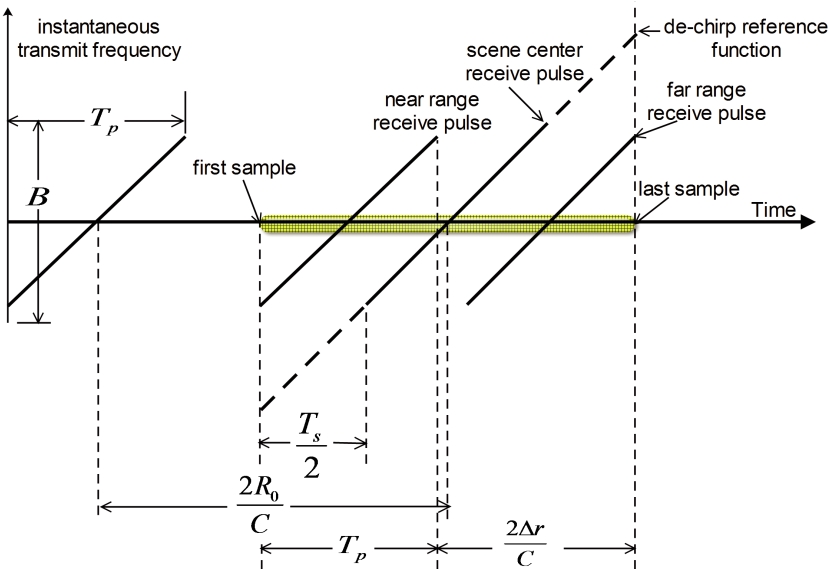

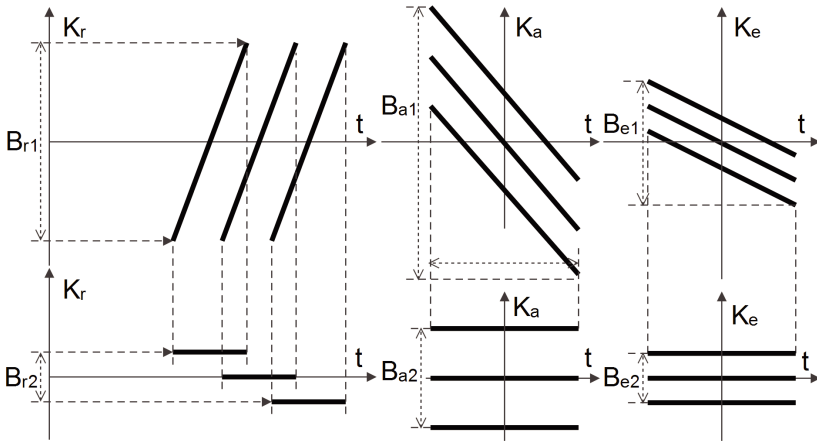**Figure 4.** Timing diagram for AD samples.

Figure 5. Echo signal bandwidth before and after dechirp processing.

The three-dimensional digitized echo signal becomes

$$S_d = a_t \sum_{m=0}^{N_e-1} \sum_{n=0}^{N_a-1} \sum_{k=0}^{N_r-1} \exp\{j\Phi(m,n,k)\}. \tag{10}$$

which encompasses N_r samples per pulse over N_a along-track pulses and N_e cross-track equivalent phase centres.

The echo signal bandwidths along wave-propagation dimension, along-track dimension and cross-track dimension before/after dechirp are compared and shown in Fig. 5.

The bandwidth along wave-propagation dimension in wave-number domain before/after dechirp is shown in Eq. (11) and Eq. (12)

$$B_{r1} = 2\pi \frac{K_r T_p}{c} \tag{11}$$

$$B_{r2} = 2\pi \frac{K_r (2w_r/c)}{c}, \tag{12}$$

where K_r is the chirp rate and T_p the pulse width of the transmitted signal. w_r is the wave-propagation dimensional range gate of the imaging scene. Bandwidth B_{r2} is only related to the wave-propagation dimensional range gate of the imaging scene.

The bandwidth along along-track dimension in wave-number

domain before and after dechirp is shown in Eq. (13) and Eq. (14)

$$B_{a1} = 2\pi \frac{2w_a}{\lambda R_t} + 2\pi \frac{2L_a}{\lambda R_t} \tag{13}$$

$$B_{a2} = 2\pi \frac{2w_a}{\lambda R_t}, \tag{14}$$

where w_a is the along-track dimensional range gate, R_t the instantaneous range form APC to target P, and L_a the length of along-track dimensional synthetic aperture. Bandwidth B_{a2} is only related to the along-track dimensional range gate of the imaging scene.

The bandwidth of cross-track dimension in wave-number domain before and after dechirp is shown in Eq. (15) and Eq. (16)

$$B_{e1} = 2\pi \frac{2w_e}{\lambda R_t} + 2\pi \frac{2L_e}{\lambda R_t} \tag{15}$$

$$B_{e2} = 2\pi \frac{2w_e}{\lambda R_t}, \tag{16}$$

where w_e is the cross-track dimensional range gate and L_e the length of cross-track dimensional linear array. Bandwidth B_{e2} is only related to the cross-track dimensional range gate of the imaging scene.

As DLSLA 3D SAR works in the mode of nadir observation, the undulation of the imaging scene is small, especially in urban areas or plain areas. From Eq. (11) to Eq. (16), we can see the echo signal bandwidth in every dimension after dechirp processing is only related with the size of the imaging scene, in this circumstance, the bandwidth is reduced enormously, especially in the wave-propagation dimension. Dechirp processing is quite suitable for DLSLA 3D SAR which possesses many receiving channels as it can reduces burden on AD converter and data collection device.

3. PROJECTION SLICE THEOREM AND ITS APPLICATION IN DOWNWARD-LOOKING SPARSE LINEAR ARRAY THREE DIMENSIONAL SAR

Several years ago, it was shown that the mathematical structure of SAR image construction is similar to the image reconstruction problem in CAT [18]. The similarity in these two otherwise seemingly different imaging systems suggested that reconstruction algorithms used in CAT could also be used in SAR [26]. In this paper we illustrate the three dimensional projection-slice theorem suited for DLSLA 3D SAR. As shown in Fig. 6, $|\overrightarrow{QO}| = R_0$, $|\overrightarrow{OP}| = R$, based on planar wave front hypothesis, range $\overrightarrow{QP}$ is $R_t = R_0 + R$. uv-plane is perpendicular to
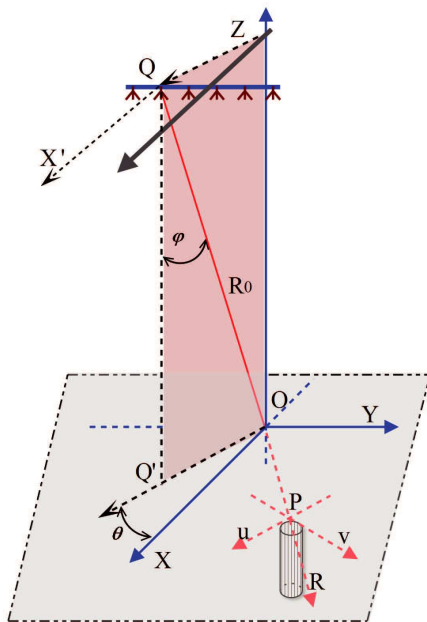
Figure 6. Three dimensional projection-slice theorem.

$\overrightarrow{QP}$, and u-axis is parallel to $\overrightarrow{OQ'}$, v-axis is perpendicular to $\overrightarrow{QP}$ and u-axis.

The dechirped 3D echo data of the whole imaging scene are obtained from the superposition of every point scatter object's echo information which also means integrating the point scatter echo obtained in Eq. (4) along u-axis, v-axis and R-axis. It can be written as

$$S_{\text{if}}(K, \varphi, \theta) = \int_R \int_u \int_v S_{\text{if}}(m, n, t) dv du dR$$

$$= \int_u \int_v \int_R f(x, y, z) \exp\{-jKR\} du dv dR, \quad (17)$$

where $f(x, y, z)$ is the complex image that we want to reconstruct, and the RVP term in Eq. (4) is not considered. According to planar wave front hypothesis, Eq. (17) can be written as

$$S_{\text{if}}(K, \varphi, \theta) = \int_u \int_v \int_R f(x, y, z) \exp\{-jKR\} du dv dR$$

$$= \int_R g(R, \varphi, \theta) dR, \quad (18)$$

where

$$g(R, \varphi, \theta) = \int_u \int_v f(x, y, z) du dv.$$

$g(R, \varphi, \theta)$ is the linear trace data along R-axis on uv plane. The dechirped 3D echo data of the whole imaging scene are the one-dimensional Fourier transform of the linear trace data $g(R, \varphi, \theta)$ along R-axis dimension.

As shown in Fig. 6, we can get that

$$\begin{bmatrix} R \\ u \\ v \end{bmatrix} = \begin{bmatrix} \cos\theta\sin\varphi & \sin\theta\sin\varphi & \cos\varphi \\ \sin\theta & \cos\theta & 0 \\ \cos\theta\cos\varphi & \sin\theta\cos\varphi & \sin\varphi \end{bmatrix} \begin{bmatrix} x \\ y \\ z \end{bmatrix} \qquad (19)$$

Substituting Eq. (19) to Eq. (17), we get

$$S_{\text{if}}(K, \varphi, \theta) = \int_u \int_v \int_R f(x, y, z) \exp\{-jKR\} \, du dv dR$$

$$= \int_x \int_y \int_z f(x, y, z) \exp\{-j\Phi_2\} |J| dx dy dz, \qquad (20)$$

where

$$\Phi_2 = KR = K(x\cos\theta\sin\varphi + y\sin\theta\sin\varphi + z\cos\varphi) = K_x x + K_y y + K_z z.$$

$|J|$ is the Jacobi's transformation determinant (according to Eq. (19), $|J| = 1$). Eq. (20) means the dechirp 3D echo data of the whole imaging scene is also the three dimensional Fourier transform of the reconstructed complex image $f(x, y, z)$ along x-axis, y-axis and z-axis dimension. This is the three dimensional projection-slice theorem for DLSLA 3D SAR. The complex image $f(x, y, z)$ we want to reconstruct can be obtained from Eq. (20) with three dimensional Inverse Fourier transform.

4. CONVOLUTION BACK-PROJECTION ALGORITHM

4.1. Three Dimensional Image Reconstruction with Convolution Back-projection Algorithm

According to Eq. (20), the complex image $f(x, y, z)$ can be reconstructed from video frequency dechirp echo signal $S_{\text{if}}(K, \varphi, \theta)$, while the flying platform motion effect during time-divided transmitting-receiving procedure should be compensated in the imaging algorithm.

The flying platform motion compensation procedure can be written as

$$S_{\text{if}}(K, \varphi, \theta) = F_x^{-1} \{F_x \{S_{\text{if}}(K, \varphi, \theta)\} \exp\{-jK_x \Delta x\}\}, \qquad (21)$$

where K_x is the along-track dimensional wave-number. Then, the three dimensional complex image $f(x, y, z)$ can be reconstructed from the flying platform motion compensated echo signal

$$f(x, y, z) = \frac{1}{8\pi^3} \iiint S_{\text{if}}(K, \varphi, \theta)|J|' \exp\{jKR\} \, dK d\varphi d\theta, \qquad (22)$$

where $|J|' = |K|^2 \sin\varphi$ is the Jacobi's transformation determinant. The inside integration can be seen as one dimensional inverse Fourier transform along R-axis. The inside integration can be written as

$$Q'(R, \varphi, \theta) = \int_{-\infty}^{\infty} S_{\text{if}}(K, \varphi, \theta)|J|' \exp\{jKR\} \, dK$$

$$= Q(R, \varphi, \theta) \exp\{-jK_c R\}, \qquad (23)$$

take consideration of sample interval

$$-\frac{T_p}{2} + \frac{2(R_0 - \Delta R)}{c} \leq t \leq \frac{T_p}{2} + \frac{2(R_0 + \Delta R)}{c}$$

$K \in [K_1, K_2]$ is obtained, where

$$K_1 = \frac{4\pi}{\lambda} - \frac{2\pi K_r}{c}\left(T_p + \frac{2\Delta R}{c}\right)$$

$$K_2 = \frac{4\pi}{\lambda} + \frac{2\pi K_r}{c}\left(T_p + \frac{2\Delta R}{c}\right).$$

If we define $K_c = \frac{4\pi}{\lambda}$ and $K_0 = \frac{2\pi K_r}{c}(T_p + \frac{2\Delta R}{c})$, then $K \in [K_c - K_0, K_c + K_0]$. As K only takes part of the space frequency band which means the dechirp echo signal is a narrow band signal, so the center frequency shifting should be considered when one dimensional inverse Fourier transform is taken [3, 19]. $Q'(R, \varphi, \theta)$ is the one dimensional inverse Fourier transform of S_{if} multiplying a filter with its spatial frequency response is $|K|^2 \sin\varphi$. So, $Q'(R, \varphi, \theta)$ can be seen as the convolution in the space domain. Then, the reconstructed complex image $f(x, y, z)$ can be written as

$$f(x, y, z) = \frac{1}{4\pi^2} \int_{-\varphi_1}^{\varphi_1} \int_{-\theta_1}^{\theta_1} Q(R, \varphi, \theta) \exp\{-jK_c R\} \, d\varphi d\theta. \quad (24)$$

For digital computer processing, the reconstructed complex image can be written as

$$f(x, y, z) = \frac{1}{4\pi^2} \sum_{ii=0}^{N_a-1} \sum_{jj=0}^{N_e-1} Q(R, \varphi_{jj}, \theta_{ii}) \exp\{-jK_c R\}\Delta\varphi\Delta\theta, \quad (25)$$

where N_a is the along-track dimensional pulse number and N_e is the equivalent phase centre number.

4.2. Convolution Back-projection Algorithm Flow

The three dimensional reconstructed complex image is the back-projection of the convolution term Q'. And, this is the convolution back-projection imaging algorithm for the DLSLA 3D SAR. For DLSLA 3D SAR, suppose the 3D imaging scene has $N_x \times N_y \times N_z$ voxel, and the coordinate of every voxel can be pre-computed before image reconstruction. During the data collection procedure, the echo signal is recorded at every digitized position of $\varphi_{jj}(jj = 1, \ldots, Ne)$ and $\theta_{ii}(ii = 1, \ldots, Na)$, and its corresponding convolution term can be computed from Eq. (23). And in Eq. (24), the convolution term of every voxel in the reconstructed formula should be interpolated from the digitized convolution term of the recorded echo signal. And the the flow diagram of convolution back-projection imaging algorithm for DLSLA 3D SAR is shown in Fig. 7. The image reconstruction procedure can be summarized as,

- Step 1. Select the 3D imaging region and compute the (x, y, z) coordinate of every voxel.
- Step 2. Read wave-propagation dimension echo data along every cross-track dimension sample φ_{jj} and every along-track dimension sample θ_{ii}.
- Step 3. Compensate the platform motion during the time-divided transmitting-receiving procedure.
- Step 4. Filter the dechirp echo signal in space frequency K domain with $|K|^2 \sin\varphi$.
- Step 5. Center frequency shift the echo signal and compute the digitized convolution term via inverse Fast Fourier transform of the filtered echo data obtained in Step 3.
- Step 6. Compute R of every voxel at cross-track dimension sample φ_{jj} and along-track dimension sample θ_{ii}.
- Step 7. Interpolate the convolution term of every voxel from the digitized convolution term obtained in Step 4.
- Step 8. Compute the back-projection data of every voxel at cross-track dimensional sample φ_{jj} and along-track dimensional sample θ_{ii}.
- Step 9. Write the binary 3D imaging result to hard disk and display the 3D imaging results.

As can be seen from the flow diagram of the convolution back-projection imaging algorithm, the main computation operations of the CBP imaging algorithm are the FFT, the complex multiplication and the interpolation. All these operations can be performed in parallel.
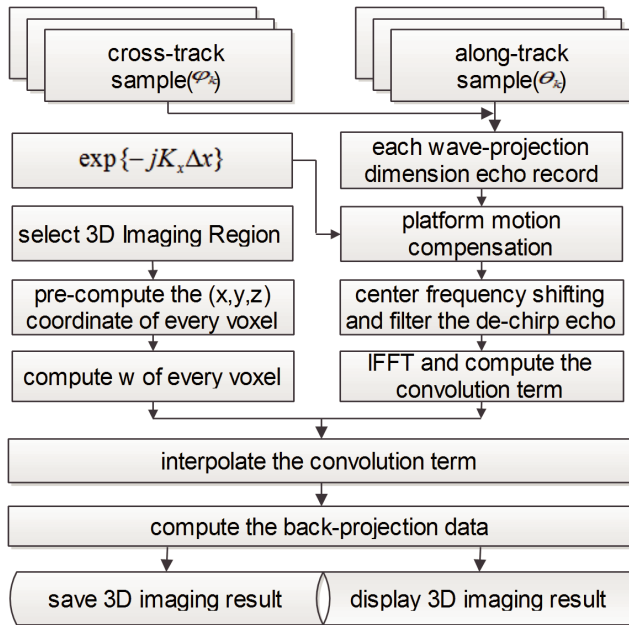
Figure 7. The flow diagram of convolution back-projection algorithm.

The computation of the back-projection procedure at every cross-track dimension sample and every along-track dimension sample can also be performed in parallel [21, 22]. Consequently, parallel implementation of the convolution back-projection imaging algorithm can be implemented in parallel on multi-core CPU platform via OpenMP or MPI (Message Passing Interface), or on GPU (Graphics processing units) platform via CUDA/OpenCL(Open Computing Language).

5. DOWNWARD-LOOKING SPARSE LINEAR ARRAY THREE DIMENSIONAL SAR COMPUTER SIMULATION

In this section, we present two numerical simulation examples based on downward-looking sparse linear array configuration to illustrate the performance of our algorithm. The parameters used in the simulation experiments are listed in Table 1. For simplicity, the losses due to the antenna pattern are not considered here. All the numerical simulations are implemented with Intel Math Kernel Library(MKL) and OpenMP on Intel(R) Core(TM) i7-2600@3.40 GHz CPU platform.

Table 1. Measurement parameters used in the simulations.

Parameters	Value
Center Frequency	37.5 GHz
Transmitting Signal Bandwidth	150 MHz
Platform Fly Height	2500 m
Platform Fly Velocity	50 m/s
Transmitting Signal Pulse Width	10 μs
AD Sampling Rate	250 MHz
Range Gate	2350–2500 m
PRF	1280 Hz
Along-track Dimension Sampling Interval	0.08 m
Transmitting Array Elements	8
Receiving Array Elements	32
Beam width of TR Array	14° (Cross-track)
Beam width of TR Array	14° (Along-track)
Equivalent Phase Center Number	256
Cross-track Dimension Sampling Interval	0.04 m

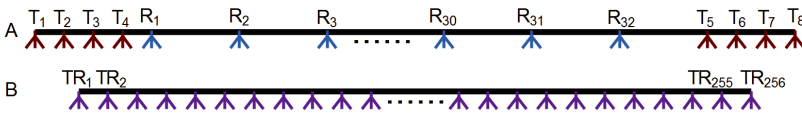where TR means Transmitting and Receiving.

Figure 8. The configuration of the sparse linear array.

Table 2. Cross-track dimensional coordinates of array elements.

Coordinates	Value (m)
Transmitting Array	$T_i = -5.18 + i \times 0.04, i \in [1, 4]$
Transmitting Array	$T_i = 5.06 + (i - 4) \times 0.04, i \in [5, 8]$
Receiving Array	$R_i = -5.02 + i \times 0.12, i \in [1, 32]$
Equivalent Array	$TR_i = -5.12 + i \times 0.04, i \in [1, 256]$

The sparse linear array we used in the simulation is composed of 8 transmitting array elements and 32 receiving array elements. The configuration of the sparse linear array is shown in Fig. 8. A is the real array distribution, B is the equivalent array distribution. The coordinates of transmitting array elements, receiving array elements and equivalent array elements is illustrated in Table 2.

In the first numerical simulation, to illustrate the capability of the reconstructed image on different height with the proposed algorithm, 3×8 point scatter objects are distributed on three circles at different height. The radius of the three circles is 40 m, 30 m, 20 m and the height of the three circles is 20 m, 40 m, 60 m, respectively. A sketch of three circles' point targets in the 3D space is shown in Fig. 9(a). The projection of the three circles onto XY plane is shown in Fig. 9(b), the projection of the three circles onto XZ plane is shown in Fig. 9(c) and, the projection of the three circles onto YZ plane is shown in Fig. 9(d). All the point scatter objects in the simulated model have the same radar cross section.

The image reconstructed by the proposed CBP imaging algorithm is shown in Fig. 10(a)–Fig. 10(d). The -19 dB iso-surface of the
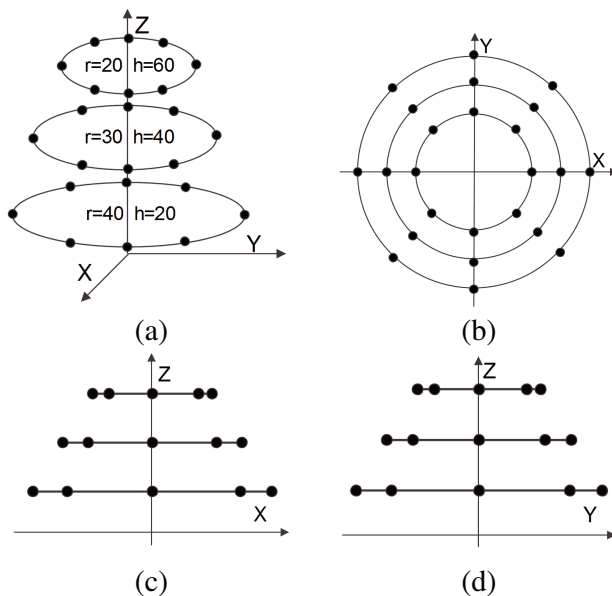

Figure 9. Simulated model of three circles' point targets. (a) Sketch of point targets. (b) Projection onto XY plane. (c) Projection onto XZ plane. (d) Projection onto YZ plane.
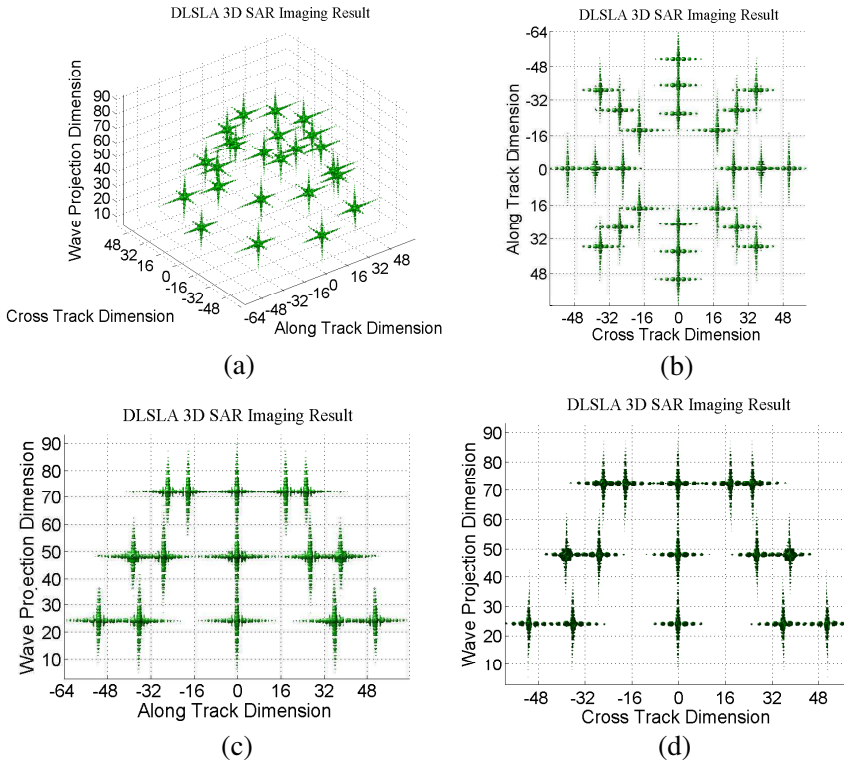
Figure 10. Reconstructed image of point targets with CBP algorithm. (a) 3D reconstructed image. (b) Projection onto XY plane. (c) Projection onto XZ plane. (d) Projection onto YZ plane.

reconstructed 3D image of point scatter objects with CBP algorithm is shown in Fig. 10(a), the projection of the reconstructed 3D image (-19 dB) onto XY plane is shown in Fig. 10(b), the projection of the reconstructed 3D image (-19 dB) onto XZ plane is shown in Fig. 10(c) and, the projection of the reconstructed 3D image (-19 dB) onto YZ plane is shown in Fig. 10(d). The reflectivity values as well as the position of the point targets are all in perfect agreement with the simulated model shown in Fig. 9(a)–Fig. 9(d).

In the second numerical simulation, an undulating hill consisting of 546 unit amplitude point scatter objects is confined in a region of size 120 mm × 120 m × 120 m. Fig. 11(a) is a sketch of the undulating hill in the 3D space. Fig. 11(b) is the projection of undulating hill onto XY plane. Fig. 11(c) is the projection of undulating hill onto XZ plane. Fig. 11(d) is the projection of undulating hill onto YZ plane. The undulating hill model is generated by a surf function in

MATLAB.

The undulating hill 3D image reconstructed with CBP imaging algorithm is shown in Fig. 12(a)–Fig. 12(d). The $-22\,$dB iso-surface of the reconstructed 3D undulating hill is shown in Fig. 12(a), the projection of the reconstructed 3D image of undulating hill ($-22\,$dB) onto XY plane shown in Fig. 12(b), the projection of the reconstructed 3D image of undulating hill ($-22\,$dB) onto XZ plane shown in Fig. 12(c), and the projection of the reconstructed 3D image of undulating hill ($-22\,$dB) onto YZ plane shown in Fig. 12(d).

In order to demonstrate the performance of the proposed imaging algorithm, the 3D resolution, the Peak Side Lobe Rates (PSLR) and the Integral Side Lobe Rates (ISLR) are all evaluated, as indicated in Table 3. The PSLR is the ratio between the height of the largest side
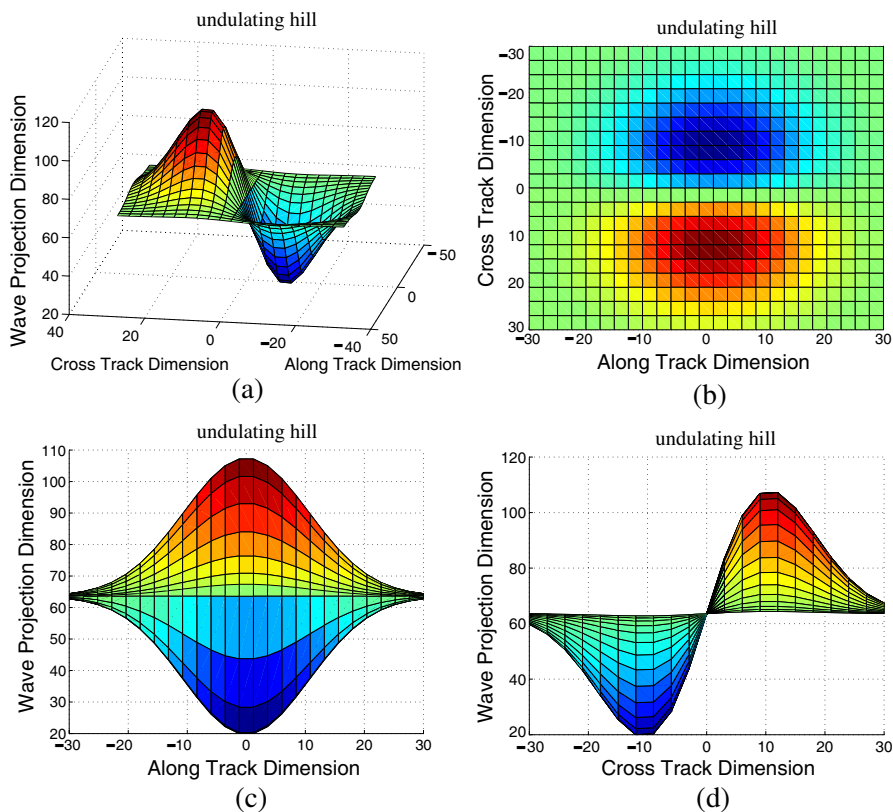

Figure 11. undulating hill model. (a) Sketch of undulating hill. (b) Projection onto XY plane. (c) Projection onto XZ plane. (d) Projection onto YZ plane.
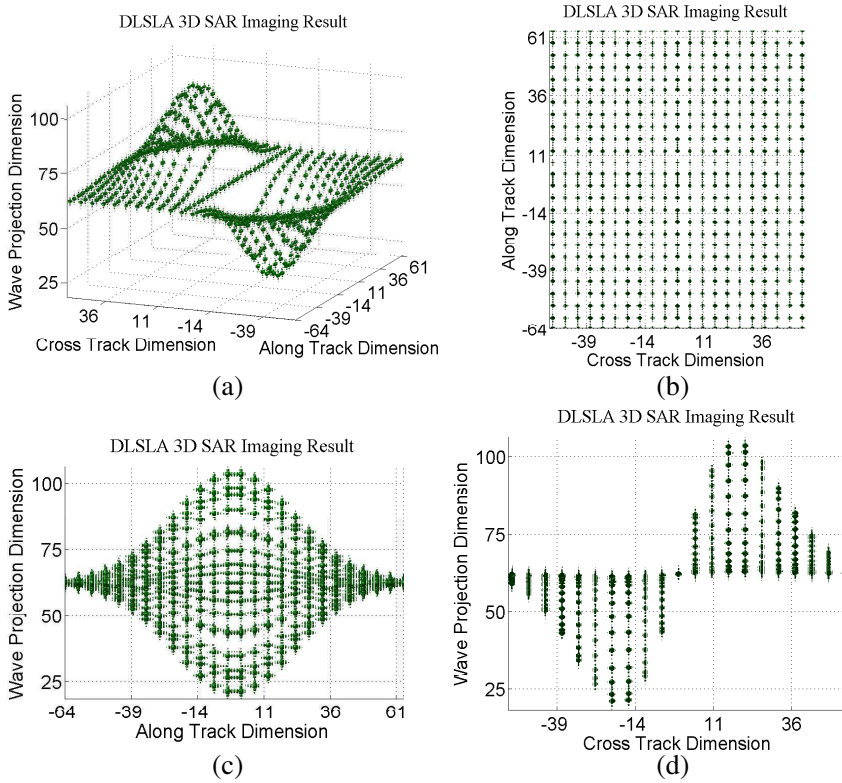
Figure 12. Reconstructed image of undulating hill with CBP algorithm (-22 dB). (a) The iso-surface of the reconstructed 3D undulasting hill (-22 dB). (b) Projection onto XY plane. (c) Projection onto XZ plane. (d) Projection onto YZ plane.

lobe A_{side} and the height of the main lobe A_{main}; that is

$$\text{PSLR} = 20\log_{10}\left\{\frac{A_{\text{side}}}{A_{\text{main}}}\right\}. \tag{26}$$

The ISLR is often used to analyse the side lobe power of point spread function (PSF). Assume that the 'main lobe' power is P_{main} and the total power is P_{total}, the ISLR is then

$$\text{ISLR} = 10\log_{10}\left\{\frac{P_{\text{total}} - P_{\text{main}}}{P_{\text{main}}}\right\}, \tag{27}$$

where the numerator is the total power of the side lobes. Usually, the null-to-null of the PSF can be defined as the main lobe width.

Figure 13 shows wave-propagation, along-track dimension, cross-track dimension profiles of a point target in Fig. 10. The profiles are used for computing PSLR and ISLR.
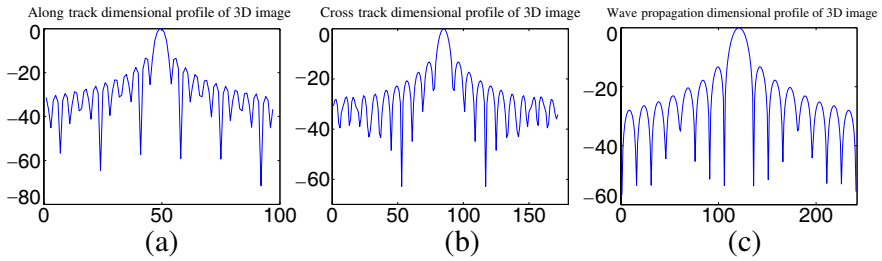
Figure 13. (a) Along-track. (b) Cross-track. (c) Wave-propagation dimension profile of the 3D image of one target obtained in the simulation 1.

Table 3. The measured PSLR, ISLR in the along-track dimension, cross-track dimension and wave-propagation dimension.

Measured Parameter	Along-track	Cross-track	Wave-propagation
PSLR (dB)	-13.52	-13.21	-13.48
ISLR (dB)	-9.89	-9.61	-10.10

6. CONCLUSION

This paper presents a 3D imaging algorithm especially tailored for accurately reconstructing the 3D image of the DLSLA 3D SAR with dechirp on receive technique. The dechirp echo signal is the three-dimensional Fourier transform of the complex image that we want to reconstruct on the basis of three dimensional projection-slice theorem. This is the kernel of projection-slice theorem and basis of our CBP imaging algorithm. Then, the convolution back-projection imaging algorithm with platform motion compensation during the time-divided transmitting-receiving procedure is deduced in detail, and the parallel implementation of the CBP imaging algorithm is discussed later. Then the algorithm is verified with two numerical simulations. The merits of the numerical reconstructed images confirm the accuracy of the proposed algorithm with DLSLA 3D SAR.

APPENDIX A. REMOVAL OF RESIDUAL VIDEO PHASE

From Eq. (4), an undesirable RVP term is a consequence of the signal dechirp on receive in the DLSLA 3D SAR. The RVP term may cause degrading and geometry distortion effects in the reconstructed image. And these effects are space-variant [2]. Sub-patch processing procedure is one way to reduce the impact of RVP while it cannot remove the RVP term completely. In this appendix, we pass the dechirp video signal through the digital equivalent of a frequency-dependent delay line and remove the RVP term completely.

$$S_{\text{if}}(m, n, t) = S_r(m, n, t) * S_{\text{ref}}(m, n, t)$$

$$= \sum_{ii=0}^{N_e-1} \sum_{jj=0}^{N_a-1} a_t \text{rect}\left(\frac{\hat{t} - t_0}{T_p}\right) \exp\left\{j\Phi\left(m, n, \hat{t}\right)\right\}, \quad \text{(A1)}$$

where

$$\Phi(m, n, \hat{t}) = \frac{4\pi K_r}{c}\left(\frac{f_c}{K_r} + \hat{t} - \frac{2R_0}{c}\right)(R_t - R_0) + \frac{4\pi K_r}{c^2}(R_t - R_0)^2. \quad \text{(A2)}$$

Assuming a positive linear FM rate, it is desirable to delay high intermediate frequencies in time relative to low video frequencies to align the signals from all point scatter objects in time. This alignment requires a frequency-dependent time delay to relate frequency by $t_d = \frac{f}{K_r}$.

This delay removes the original echo time delay difference between signals from different ranges. Application of new delay introduces a multiplicative term of phase $\frac{-\pi f^2}{K_r}$ into the original signal and removes RVP term from the signal history.

Taking the time derivative of Eq. (A2), the instantaneous frequency is

$$f = \frac{1}{2\pi}\frac{d\Phi}{d\hat{t}}. \quad \text{(A3)}$$

As $R = R_t - R_0$, relative to effects of time delay of $t_d = \frac{f}{K_r}$, evaluating this derivative yields the approximation

$$f \approx -\frac{2K_r}{c}R, \quad \text{(A4)}$$

is adequate. It is indicated that scatters that are nearer than R_0 have a positive frequency in this representation while those that are distant have a negative frequency. The result of passing the signal of phase Φ
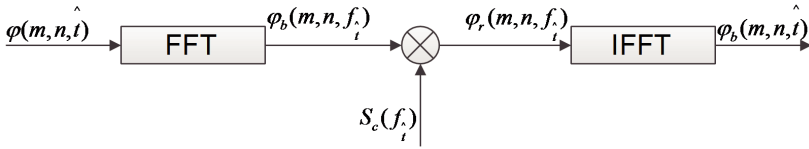
Figure A1. The flow diagram of RVP term elimination.

through the delay line with $t_d = \frac{f}{K_r}$ is the new phase $\Phi_r = \Phi - \frac{\pi f^2}{K_r}$, which, on substitution of the expression in Eq. (A4) for f, becomes

$$\Phi_r(m, n, \hat{t}) = -\frac{4\pi K_r}{c}\left(\hat{t} - \frac{2R_a}{c} + \frac{f_c}{K_r}\right) R. \tag{A5}$$

This expression is the desired phase for a target R_t and reference range R_0. The RVP term has been eliminated. Fig. A1 illustrates the block diagram of the RVP term elimination procedure. The procedure involves a Fourier transform, a complex multiply and an inverse Fourier transform. where

$$S_c(f_{\hat{t}}) = \exp\left\{-j\frac{f_{\hat{t}}^2}{K_r}\right\}. \tag{A6}$$

REFERENCES

1. Soumekh, M., *Synthetic Aperture Radar Signal Processing with Matlab Algorithms*, John Wiley & Son, 1999.
2. Carrara, W. G., R. S. Goodman, and R. M. Majewski, *Spotlight Synthetic Aperture Radar: Signal Processing Algorithms*, Artech House, 1995.
3. Jakowatz, C. V., D. E. Wahl, P. H. Eichel, D. C. Ghiglia, and P. A. Thompson, *Spotlight-mode Synthetic Aperture Radar: A Signal Processing Approach*, Kluwer Academic Publishers, Boston London Dordrecht, 1996.
4. Weib, M. and J. H. G. Ender, "A 3D imaging radar for small unmanned airplanes-ARTINO," *EURAD*, 209–212, 2005.
5. Gierull, C. H., "On a concept for an airborne downward-looking imaging radar," *International Journal of Electronics and Communications*, Vol. 53, No. 6, 295–304, 1999.
6. Nouvel, J. F., S. Roques, and O. R. Du Plessis, "A low-cost imaging radar: DRIVE on board ONERA motorglider," *IGARSS*, 5306–5309, 2007.

7. Nouvel, J. F., S. Angelliaume, and O. R. Du Plessis, "The ONERA compact Ka-SAR," *EuRAD*, 475–478, 2008.

8. Du Plessis, O. R., J. F. Nouvel, R. Baque, G. Bonin, P. Dreuillet, C. Coulombeix, and H. Oriot, "ONERA SAR facilities," *RADAR*, 667 –672, 2010.

9. Klare, J., M. Weib, O. Peters, A. R. Brenner, and J. H. G. Ender, "ARTINO: A new high resolution 3D imaging radar system on an autonomous airborne platform," *IGARSS*, 3842–3845, 2006.

10. Weib, M. and M. Gilles, "Initial ARTINO radar experiments," *EUSAR*, 857–860, 2010.

11. Wei, S. J., X. L. Zhang, and J. Shi, "Linear array SAR imaging via compressed sensing," *Progress In Electromagnetics Research*, Vol. 117, 299–319, 2011.

12. Du, L., Y. P. Wang, W. Hong, and Y. R. Wu, "Analysis of 3D-SAR based on angle compression principle," *IGRASS*, 1324–1327, 2008.

13. Zhu, X. X. and R. Bamler, "Tomographic SAR inversion by-Norm regularization the compressive sensing approach," *IEEE Transactions on Geoscience and Remote Sensing*, Vol. 48, No. 10, 3839–3846, 2010.

14. Qu, Y., G. Liao, S. Q. Zhu, X. Y. Liu, and H. Jiang, "Performance analysis of beamforming for MIMO radar," *Progress In Electromagnetics Research*, Vol. 84, 123–134, 2008.

15. Solimene, R., A. Brancaccio, R. Di Napoli, and R. Pierri, "3D sliced tomographic inverse scattering experimental results," *Progress In Electromagnetics Research*, Vol. 105, 1–13, 2010.

16. Ren, X. Z., L. H. Qiao, and Y. Qin, "A three-dimensional imaging algorithm for tomography sar based on improved interpolated array transform," *Progress In Electromagnetics Research*, Vol. 120, 181–193, 2011.

17. Natterer. F., *The Mathematics of Computerized Tomography*, John Wiley & Sons, 1986.

18. Munson, J. D. C., J. D. O'Brien, and W. K. Jenkins, "A tomographic formulation of spotlight-mode synthetic aperture radar," *Proceedings of the IEEE*, Vol. 71, No. 8, 917–925, 1983.

19. Desai, M. D. and W. K. Jenkins, "Convolution backprojection image reconstruction for spotlight mode synthetic aperture radar," *IEEE Transactions on Image Processing*, Vol. 1, No. 4, 505–517, 1992.

20. Knaell, K. K. and G. P. Cardillo, "Radar tomography for the generation of three-dimensional images," *IEE Proceedings on*

Radar, Sonar and Navigation, Vol. 142, No. 2, 54–60, 1995.

21. Tao, Y. B., H. Lin, and H. J. Bao, "From CPU to GPU: GPU-based electromagnetic computing (GPUECO)," *Progress In Electromagnetics Research*, Vol. 81, 1–19, 2008.

22. Dziekonski, A., A. Lamecki, and M. Mrozowski, "A memory efficient and fast sparse matrix vector product on a GPU," *Progress In Electromagnetics Research*, Vol. 116, 49–93, 2011.

23. Perez Lopez, J. R. and J. Basterrechea, "Hybrid particle swarm-based algorithms and their application to linear array synthesis," *Progress In Electromagnetics Research*, Vol. 90, 63–74, 2009.

24. Zaharis, Z. D. and T. V. Yioultsis, "A novel adaptive beamforming technique applied on linear antenna arrays using adaptive mutated boolean PSO," *Progress In Electromagnetics Research*, Vol. 117, 165–179, 2011.

25. Huang, Y., P. V. Brennan, D. Patrick, I. Weller, P. Roberts, and K. Hughes, "FMCW based mimo imaging radar for maritime navigation," *Progress In Electromagnetics Research*, Vol. 115, 327–342, 2011.

26. Demirci, S., H. Cetinkaya, E. Yigit, D. Ozdemir, and A. Vertiy, "A study on millimeter-wave imaging of concealed objects: Application using back-projection algorithm," *Progress In Electromagnetics Research*, Vol. 128, 457–477, 2012.